communications earth & environment

Article

https://doi.org/10.1038/s43247-024-01480-x

Seafloor roughness reduces melting of East Antarctic ice shelves

Yuhang Liu [1,2], Maxim Nikurashin [1,2,3,4] & Beatriz Peña-Molino [2,5]

Heat delivered by the ocean circulation is melting the Antarctic ice sheet from below. This melt is largest where warm Circumpolar Deep Water accesses the continental shelf and reaches the ice shelf cavities. Future melt rate projections are based on ocean thermal forcing derived from climate models, which tend to be biased warm around Antarctica. The bias has been attributed to unresolved ocean processes that occur at scales poorly represented in models. Using a high-resolution model of the Denman Glacier region we show that seafloor roughness unresolved in climate models suppresses the impact of warm water on ice sheet melting. Seafloor roughness slows down the shelf circulation, reducing the presence of warm water over the shelf and the heat transport towards the ice cavities. As a result, the total meltwater discharge drops by 4 Gt year^{-1}. Our results suggest a mechanism missing in global ocean and climate models that could reduce the spread in climate projections.

Projections of global mean sea level rise range from 0.28–0.55 m and 0.44–0.76 m rise by the end of the century for the low and high emissions scenarios, respectively[1]. The large spread in sea level rise estimates results from a poorly constrained future contribution of the Antarctic ice sheet. Estimates of meltwater input from Antarctica are derived from ice sheet models driven by ocean thermal forcing obtained from global climate models[2,3]. Climate models predict warming of the deep continental shelf waters around Antarctica by the end of the century[4,5]. However, these models are biased warmed around Antarctica[5,6] and show other biases in the subpolar large-scale ocean circulation and its response to climate change[7,8]. These biases are attributed to the coarse resolution of climate models and partly explained by a poor representation of a wide range of dynamical processes in the ocean near Antarctica[2,9]. Thus, it is crucial to improve our understanding of how unresolved processes control the ocean properties around Antarctica[10].

Unlike West Antarctica, East Antarctica has been relatively stable[11]. However, studies suggest that the Denman Glacier, the second largest contributor to ice mass loss in East Antarctica[12,13] located at 98°E, has been changing rapidly in recent decades[12–16]. As in West Antarctica, mass loss from the East Antarctic ice sheet[17–19] has been attributed to the presence of Circumpolar Deep Water (CDW) in the adjacent continental shelf[20–23]. The transport of CDW towards the ice shelf cavities where melting occurs can be described by two stages. First, CDW must cross the continental slope. Once on the continental shelf CDW occupies the depth range of 400–500 m, where it mixes with the surrounding water to produce modified Circumpolar Deep Water (mCDW)[24,25]. In the second stage, mCDW must be transported towards the ice shelf cavities[17,23]. Each of these stages is associated with a 'barrier', a feature of the circulation that prevents the heat from advancing poleward. The margins around most of East Antarctica, including the Denman region, can be described as a Fresh Shelf[26], where the continental shelf water is fresher than waters in the Southern Ocean, and a strong density front known as the Antarctic Slope Front (ASF) separates the two water masses. The flow along the ASF is directed westward, in a more or less coherent current known as the Antarctic Slope Current (ASC). The ASF and the ASC are the first barriers to cross-slope transport[26,27]. The main processes that can break this barrier and lead to intrusions of CDW are eddies[26,28,29] and tides[26,30,31]. Further onshore, the Antarctic Coastal Current (AACC), a westward current flowing along the coast[32,33], plays a similar role as a barrier for the local mCDW access to the ice shelf cavities. Here too eddies and tides are responsible for transporting heat across the current[34,35]. Alternatively, the AACC may also provide a pathway for warm anomalies from upstream sources to reach the ice shelf cavity[36,37]. The ASC, AACC, and the associated eddies are highly variable in space and time[26,38–40]. Understanding how this complex circulation at the continental slope and shelf, consisting of mean circulation, eddies, and tides, work collectively to prevent or facilitate the supply of heat towards the ice shelf cavity of the Denman Glacier will be critical to predict its future evolution.

Another important factor that controls the supply of heat towards the ice shelves is bathymetry. The Antarctic margin circulation is deep-reaching and thus strongly influenced by bathymetry[37]. Across the continental slope, the rapid change in bathymetry provides a dynamical constraint to cross-slope heat transport[20], since the ASC must flow along isobaths in order to conserve potential vorticity. Canyons and abrupt changes in the seabed found at the shelf break can support cross-slope flows and thus break this

[1]Institute for Marine and Antarctic Studies, University of Tasmania, Hobart, TAS, Australia. [2]Australian Antarctic Program Partnership, University of Tasmania, Hobart, TAS, Australia. [3]ARC Centre of Excellence for Climate Extremes, University of New South Wales, Sydney, NSW, Australia. [4]Australian Centre for Excellence in Antarctic Science, Hobart, TAS, Australia. [5]CSIRO Environment, Hobart, TAS, Australia. e-mail: bea.pena-molino@csiro.au

dynamical barrier[20,22,41–43], as well as generate internal waves and lead to mixing[20]. The impact of bathymetry over the continental shelf on the circulation, water mass properties, and heat transports is much less understood. Troughs have been suggested to act as conduits for mCDW towards ice shelf cavities[44,45]. A modelling study in Prydz Bay, East Antarctica[37], using bathymetry corrected with bottom depths derived from in-situ hydrographic observations, shows that a large-scale seafloor feature upstream of the Amery Ice Shelf re-routes the coastal current, thus making a strong impact on the heat transport towards the ice shelf. Similarly, inclusion of a ridge blocks deep inflow from the Bellingshausen Sea, leading to enhanced heat transport on the continental shelf in the Amundsen Sea region[46]. In Prydz Bay the corrected bathymetry also indicates the presence of small, horizontal scales smaller than 100 km, scale seafloor roughness throughout the shelf[37]. Similar seafloor roughness has also been found in other regions of the Antarctic continental shelf[47,48]. Seafloor roughness in ocean basins, referred to as abyssal hills[49], has been found to play an important role for the circulation and properties in the ocean in two ways. First, it applies a drag in the form of topographic form stress[50] to the deep-reaching currents and eddies in the Southern Ocean, having an impact on their magnitude[51–53] and sensitivity to wind[54,55]. Second, the interaction between abyssal hills and deep currents, eddies, and tides generates small-scale internal waves that radiate away, break, and drive mixing, transforming water masses in the ocean interior[56–58]. Seafloor roughness and the motions it generates are not resolved by most global ocean and climate models, nor are they systematically parameterised. The impact of the seafloor roughness on the circulation and water mass properties over the Antarctic shelf, and its implications on ice shelf melting, have not been explored.

Direct bathymetry observations over the Antarctic continental shelf are limited and completely lacking in some remote locations under permanent ice cover[59,60]. Satellite-based bathymetry still constitutes the main data available for large portions of the Antarctic margin, and in particular, the Denman region[14,16]. However, small-scale seafloor features are not resolved by satellite gravity[61]. Currently, several global and regional bathymetry datasets covering the Denman region are available and have been used in modelling and observational studies. Here, we focus on two datasets, BedMachine Antarctica Version 2 (BedMachine, hereafter) and Shuttle Radar Topography Mission at 15 arc sec resolution (SRTM15). BedMachine is a compilation of the sea bed topography and ice thickness in Antarctica[60,62]. It is one of few products that provide geometry of ice shelf cavities and sub-ice bathymetry, and hence it is widely used in Antarctic margin studies[12,26]. Ocean bathymetry in BedMachine is derived from the International Bathymetric Chart of the Southern Ocean (IBCSO)[63], which is restricted to large-scale bathymetry and thus has a fairly smooth representation of the Antarctic continental slope and shelf regions (Fig. 1a). The second product, SRTM15, is a high-resolution ocean-only bathymetry produced by combining satellite-based bathymetry with available ship soundings[64] (Fig. 1b). SRTM15 has been widely used in global ocean modelling, e.g., the barotropic tide model (TPXO9), and has recently been added as a bathymetry data source to IBCSO Version 2[65]. Comparing BedMachine bathymetry and SRTM15, the most striking difference is the ubiquitous small-scale seafloor roughness present over the shelf in SRTM15, but not in BedMachine (Fig. 1c). The variance at 10–60 km scales is up to an order of magnitude different between the two products, with seafloor roughness in SRTM15 being consistent with multi-beam soundings collected in the Vincennes Bay to the East of Denman Glacier (Supplementary Note 1). Thus, by running and comparing model simulations with the two bathymetry products we can assess the impact of small-scale seafloor roughness on the Antarctic margin circulation and ice shelf melting.

To this end, we present results from high-resolution regional ocean model simulations of the Denman Glacier region (Fig. 2a) simultaneously resolving currents, eddies, and tides, configured with thermodynamic ice shelf cavities and run with two publicly available bathymetry products under identical configurations. Specifically, the model has roughly 1.4 km horizontal resolution and 160 vertical levels, with 100 vertical levels in the top 1 km to represent the continental shelf. The model is forced by the 3-hourly atmospheric forcing derived from the Japanese 55-year atmospheric reanalysis (JRA55v1.3)[66] at the surface. At the open boundaries, the model is restored to monthly-mean fields from the 1990-91 repeat-year ACCESS-OM2-01 run[67] and also forced by TPXO9v4 barotropic tide velocities for 10 tidal constituents. The model simulations are run for 10 years, reaching equilibrium after the first 5 years, and the last 5 years of the model outputs are used for analysis. Additional details of the model configuration are given

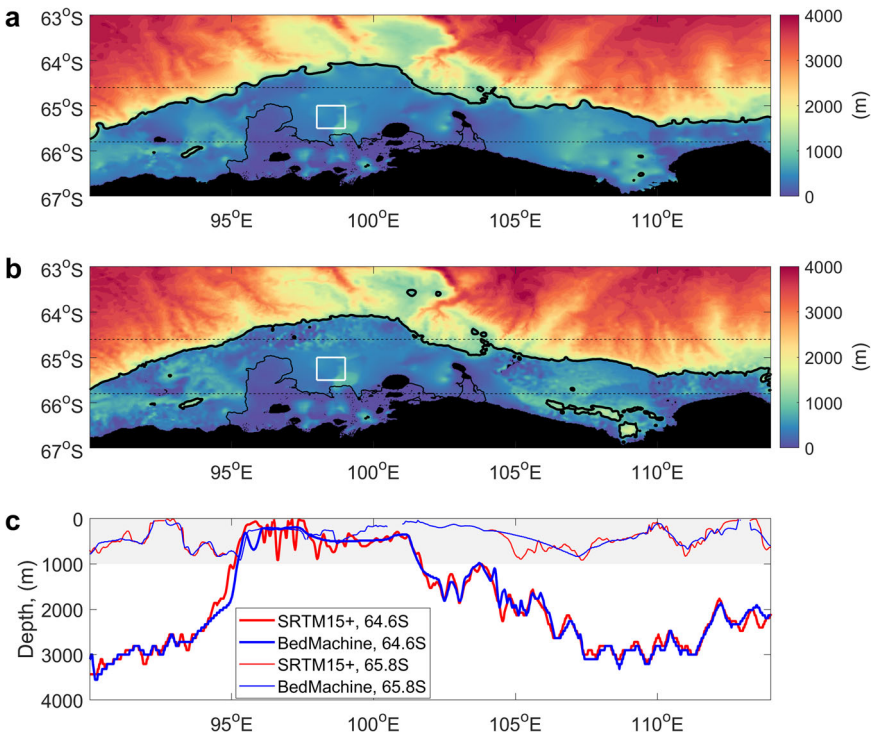

Fig. 1 | Regional bathymetry. A map of bathymetry in (m) from (**a**) BedMachine and (**b**) SRTM15 datasets. (thin black) Ice shelf boundary and (thick black) 1000 m isobath are shown. The region used for the TS diagram calculation in Fig. 4. is shown by the white box. BedMachine bathymetry is used in both simulations in a region around the ice shelf (94.5-104°E, 64.8-67°S). **c** Zonal profiles of bathymetry in (m) from (blue) BedMachine and (red) SRTM15 datasets at (thick) 64.6°S and (thin) 65.8°S indicated with dashed lines in (**a**) and (**b**). A characteristic continental shelf depth of 1000 m is shaded in grey.

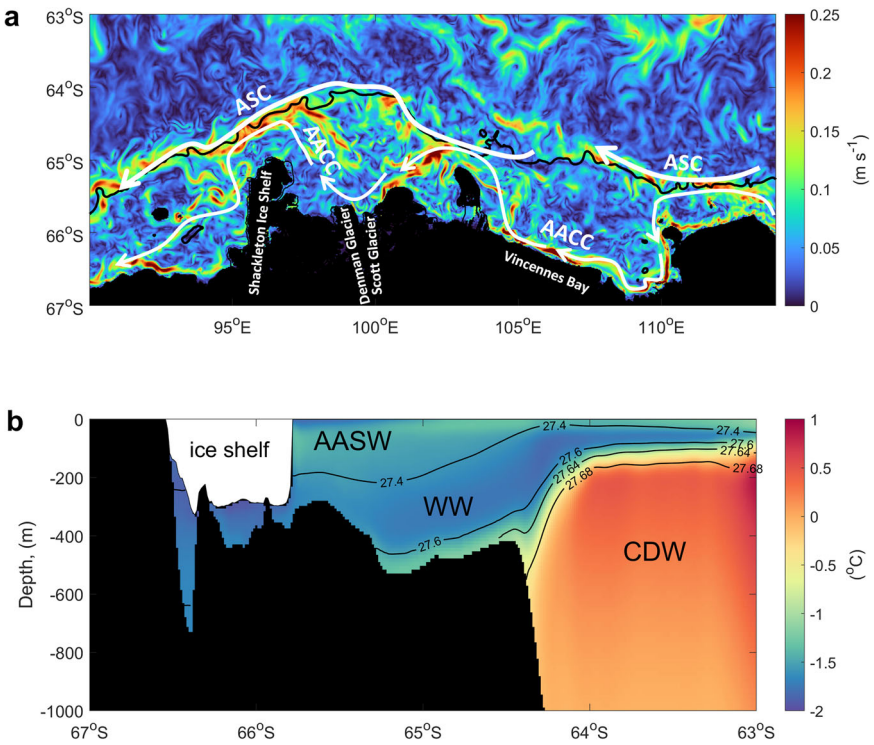

Fig. 2 | Regional surface currents and water masses. a A snapshot of the ocean current speed in ($m\ s^{-1}$) at 100 m depth at the end of the BedMachine simulation. (thin black) Ice shelf boundary, (thick black) 1000 m isobath, and (thick arrow) ASC and (thin arrow) AACC pathways are shown. **b** Time-averaged vertical and meridional section of temperature in (°C) at 98°E. Black contours show isopycnals in ($kg\ m^{-3}$).

in the Methods and the model validation with available observations is presented in Supplementary Note 2. There are some differences between the two bathymetry products also at large scales, which may potentially have an impact on our results. To attribute our results to small-scale seafloor roughness, we carried out two additional simulations by adding synthetic small-scale roughness to the BedMachine product (Supplementary Note 3). These additional simulations have the same large-scale (60 km horizontal scale and larger) bathymetry as in BedMachine, thus allowing us to directly attribute the impacts to the small-scale seafloor roughness (10–60 km horizontal scales). The additional simulations are presented in the Supplementary Note 4.

Results

We define the BedMachine simulation as our reference run and assess the impact of small-scale seafloor roughness by comparing it to the SRTM15 simulation. We also define the box in front of the glacier, in which bathymetry is identical between the two simulations, as our control region for comparing water mass properties. The reference (BedMachine) model simulation captures a range of features of the regional ocean circulation, including the ASC, AACC, and eddies (Fig. 2a). The ASC tends to follow the continental slope; it has speeds of up to 0.2 $m\ s^{-1}$ and is strongly eddying. The AACC follows the coastline and the ice shelf boundary, which are roughly 100–200 km south of the continental shelf break in this region. In Vincennes Bay, the AACC is narrow and fairly continuous with speeds exceeding 0.3 $m\ s^{-1}$. Elsewhere, the AACC appears less coherent and weaker. The reference model annual-mean temperature ranges from cold, −2 to −1.5 °C, over the continental shelf to relatively warm, about 0 °C, in the Southern Ocean (Fig. 2b). A strong temperature (and density) gradient at the shelf break corresponds to the westward ASC. At the bottom of the continental shelf relatively warm (−1 °C) water stretches from the shelf break towards the ice shelf boundary. This is the signature of CDW intrusions, coming from the Southern Ocean onto the continental shelf and modified through mixing with shelf waters[68]. In the following sections, we describe various diagnostics to characterise the regional circulation, water masses, quantify their impact on the ice shelf melting, and examine how they change in response to seafloor roughness.

Regional circulation

We use kinetic energy and volume transport to quantify the ocean circulation in this region and its response to seafloor roughness. The circulation is dominated by more or less coherent currents and eddies both variable over a wide range of scales. To quantify the relative magnitude of the various components of the ocean circulation and their variability, we decompose the total kinetic energy (KE) into mean (MKE), seasonal (SKE), and eddy (EKE) kinetic energy components as described in the Methods (Fig. 3). In this definition, EKE includes all variability other than seasonal, and hence also includes tides.

In the BedMachine simulation, around 2 Sv of water enters the domain through the eastern boundary, flows along the continental shelf, and leaves the domain through the western boundary. Following the overall direction of the time-mean circulation from east to west, the ASC flows along the shelf break, while the AACC meanders between the coast and shelf break. In Vincennes Bay, the ASC enters from the east and then splits around 110°E with approximately half of its transport (1–1.5 Sv) turning sharply towards the coast to feed the AACC (Fig. 3a). The rest of the ASC continues westward along the continental slope. The time-mean ASC and AACC are fairly strong and coherent along the entire continental shelf. In comparison, in the SRTM15 simulation (Fig. 3d), the AACC mean kinetic energy is less than half of that in the BedMachine simulation and its transport is also significantly reduced. The overall mean zonal transport through the continental shelf (onshore of the 1000 m isobath) is reduced from 2 Sv in the BedMachine simulation to 1.5 Sv in the SRTM15 simulation. Thus, seafloor roughness has an impact on the time-mean circulation through changes in the partitioning between the ASC and AACC.

While the time-mean circulation is dominated by the ASC, the seasonal variability is strongest in the AACC in both simulations (Fig. 3b, e). This likely results from the seasonal cycle in sea ice in two ways. Firstly, active sea ice formation homogenises shelf water in the vertical through convection. Secondly, sea ice insulates the ocean below from easterly winds. While the sea ice extends north of the continental shelf into the Southern Ocean, the sea ice cycle has a stronger effect on the AACC, as the ASC is also driven by the basin scale interior density gradient between the Southern Ocean and shelf waters, and hence is less influenced by the sea ice extent in winter.

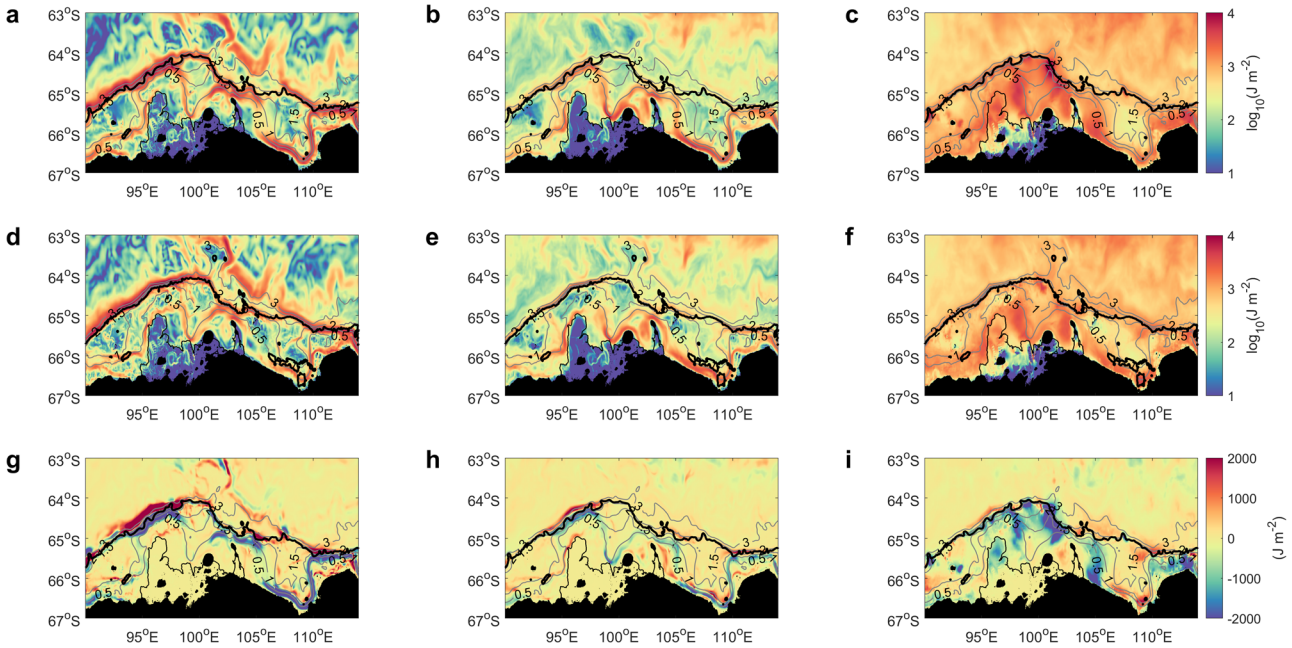

Fig. 3 | Kinetic energy of the ocean circulation. a, **b**, **c** Time-averaged kinetic energy integrated over top 1000 m in $\log_{10}$(J m^{-2}) from the BedMachine simulation and (**d**, **e**, **f**) from the SRTM15 simulation. **g**, **h**, **i** Kinetic energy difference in (J m^{-2}) between the SRTM15 and BedMachine simulations. (**a**, **d**, **g**) Mean, (**b**, **e**, **h**) seasonal, and (**c**, **f**, **i**) eddy kinetic energy components. (thin black) Ice shelf boundary, (thick black) 1000 m isobath, and (thin grey) vertically-integrated transport in (Sv) are shown.

In the presence of seafloor roughness, the seasonal variability changes in a similar way to the time-mean circulation. The kinetic energy of seasonal variability of the AACC is reduced and shifts further away from the coastline in the SRTM15 simulation, while it is slightly increased along the ASC (Fig. 3h).

Finally, for all other time scales, the distribution of EKE shows that variability tends to be enhanced over the shelf along the AACC pathway in both simulations (Fig. 3c, f). In particular, EKE is the largest where the flow becomes predominantly meridional, possibly becoming unstable to baroclinic instability and leading to enhanced variability and generation of eddies[69]. Around the northern tip of the ice shelf at 97°E and 103°E, the AACC merges with the ASC leading to enhanced variability and eddies in this region. Seafloor roughness has a strong effect on the EKE as shown by the SRTM15 simulation (Fig. 3f). A major difference between the two simulations is in front of the ice shelf, where the EKE is strongly suppressed in the SRTM15 simulation. The suppression of EKE in this region could be a combination of the impact of seafloor roughness on eddies as well as the reduced instability of the AACC due to its weaker mean and seasonal components. Eddies over the Antarctic margins have previously been found to be sensitive to the degree of topography smoothing in a modelling study of the Ross Sea, West Antarctica, using IBCSO ocean bathymetry[70].

The two additional simulations, in which synthetic seafloor roughness at 10–60 km scales is added to BedMachine bathymetry (Supplementary Note 3 and 4), show qualitatively and quantitatively similar results, confirming that the difference between the circulation in BedMachine and SRTM15 can be attributed to seafloor roughness. In summary, the small-scale seafloor roughness over the continental shelf has a significant impact on the ocean circulation. The strength of the mean and seasonal components of the AACC is reduced in the SRTM15 simulation, while the strength of the mean ASC component is increased. The EKE over the shelf is generally suppressed in the SRTM15 simulation. The response of the ocean circulation to seafloor roughness over the continental shelf is consistent with the results and mechanisms described in previous studies of the Southern Ocean[50,71], showing that seafloor roughness applies a drag to the deep-reaching currents and eddies leading to a decrease in their kinetic energy. In the SRTM15 simulation, the AACC experiences a stronger drag from seafloor roughness over the shelf, and becomes weaker and less efficient at transporting water westward across the region. To compensate, the ASC intensifies, transporting more water along the continental slope.

Water mass properties over the shelf

The ocean circulation at the shelf break and over the shelf is believed to modulate the transport of CDW onto the shelf and hence it can impact water mass properties over the shelf. To assess this impact, we focus on the control region, where the bathymetry is identical between the simulations and thus the difference cannot be attributed to local changes in bathymetry. The temperature-salinity (TS) diagram in the BedMachine simulation shows three distinct water masses (Fig. 4a): Antarctic Surface Water (AASW), Winter Water (WW) and mCDW. Most of the spread in properties occurs within the AASW (density roughly below 27.4 kg m^{-3}) which tends to occupy depths above 200 m. AASW is in contact with the atmosphere and its properties change throughout the year. Different branches of the AASW properties, having similar salinity and density but different temperatures, correspond to different seasons. Beneath the AASW, there is the WW (density range of 27.4–27.6 kg m^{-3}) occupying roughly 200–400 m depth range and having a tighter property distribution. This water mass is locally produced by winter time convection and hence is saltier and colder than the AASW. Finally, the deepest layer near the Denman Glacier, 400–600 m, is occupied by relatively warm and salty mCDW (density greater than 27.6 kg m^{-3}). Overall, the water mass properties, including the mCDW, over the shelf in the reference model are consistent with the limited observations in the region[44] (Supplementary Note 2).

To characterise the water mass composition over the shelf and quantify changes in response to seafloor roughness we use a volumetric TS diagram, that is, we compute water mass volumes for a range of temperature and salinity bins. We show the difference between the volumetric diagrams computed for each simulation (Fig. 4b) and integrate volumes for the three major water masses defined by their potential density ranges. In the BedMachine simulation, most of the volume in our control region is occupied by AASW and WW, 31% and 62%, respectively. The mCDW accounts for a smaller fraction, 7%. In response to seafloor roughness, the volume of mCDW reduces to 1% in the SRTM15 simulation in the control region.

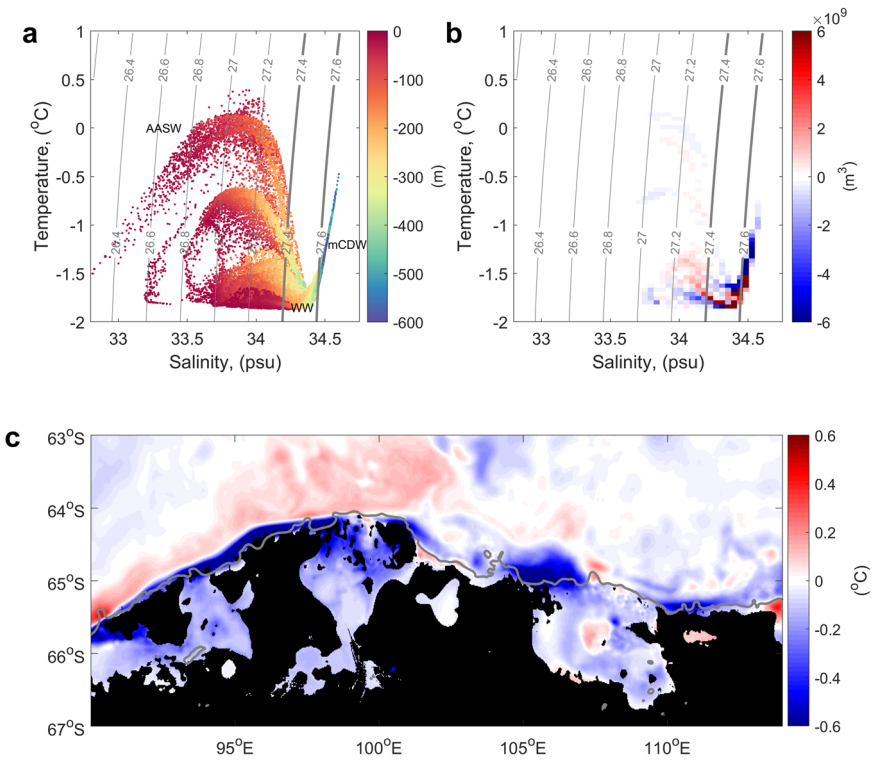

Fig. 4 | Water mass properties. a Temperature-salinity (TS) diagram from the BedMachine simulations. The colour shows depth and contours show potential density in (kg m^{-3}) referenced to 0 m depth. **b** Difference between the volumetric TS diagrams for the SRTM15 and BedMachine simulations. Positive (negative) values correspond to the volume increase (decrease) in the SRTM15 simulation. **c** Time-averaged temperature difference at 400 m depth in (°C) between the SRTM15 and BedMachine simulation. Positive (negative) values correspond to the temperature increase (decrease) in the SRTM15 simulation. (black) Ice shelf boundary and coastline and (thick grey) 1000 m isobath.

This change is compensated by a 7% increase in the volume of the WW. Changes in the volume of the AASW between simulations are negligible, 1%, as this water mass is largely controlled by surface processes and hence is insensitive to seafloor roughness. The main impact of seafloor roughness is at depth, where mCDW and WW are found.

This difference in properties at depth between the two simulations is not restricted to our control region, but affects the entire continental shelf. The shelf temperature at 400 m depth decreases by up to 0.1–0.2 °C over the shelf and under the ice shelf and by up to 1 °C at the shelf break (Fig. 4c). The strongest cooling occurs at the shelf break at 105–107°E and west of roughly 100°E, both regions characterised by large changes in the mean ASC position indicated by positive and negative anomalies in the MKE difference between the simulations (Fig. 3g) caused likely by difference in large-scale bathymetry between the two bathymetry products. However, our additional simulation with synthetic small-scale roughness over the shelf (Supplementary Note 4), shows a similar decrease in the shelf temperature by 0.1–0.2 °C over most of the shelf, confirming that the impact on temperature over the shelf can be attributed to seafloor roughness.

Ocean heat transports and distribution over the shelf

Changes in the circulation and water masses in response to seafloor roughness have an impact on heat transport and heat distribution over the shelf. To quantify how much of this heat is available and can be supplied to the ice shelf cavity by the ocean circulation, we estimate the divergence of the ocean heat transport over the continental shelf. Integrated over the entire continental shelf, a net convergence of heat would result from intrusions of CDW. These intrusions can cross the shelf break locally or remotely and be advected into the domain through the lateral boundaries. Once on the shelf, the spatial distribution of the divergence is controlled by the combined effect of transformation of CDW by mixing and its advection by the shelf circulation, including the AACC and eddies. Our results from the BedMachine simulation show that there is an overall convergence (i.e., negative heat flux divergence) of the ocean heat transport on the shelf (Fig. 5a), implying warming of the shelf waters by the ocean heat fluxes due to horizontal advection. This warming can be balanced locally by the air–sea fluxes as well as sea ice and ice shelf melting. The heat flux convergence is strongest along the path of the AACC near the coast and along the ice front with magnitudes of up to 50–60 W m^{-2}. The heat convergence is more spread in regions of strong EKE, directly opposite to the Denman ice front and is generally weak along the outer portion of the continental shelf near the shelf break. In the SRTM15 simulation, the heat convergence over the shelf is generally reduced (Fig. 5b) by up to 20 W m^{-2} near the coast and ice shelf in the western half of the domain, and increased by as much in the outer portion of the shelf along the shelf break and in Vincennes Bay (Fig. 5c). Moreover, there is a reduction of the heat flux convergence under most parts of the ice shelf. Thus, the results show that there is a redistribution—a shift to the outer and upstream portion of the shelf—of the heat flux convergence in response to seafloor roughness. This change in the ocean heat distribution over the shelf is consistent with the changes of the AACC, generally leading to reduced westward heat advection over the shelf as discussed above.

Next, we integrate the heat convergence over the continental shelf region defined by the 1000 m isobath and east and west boundaries at 90°E and 114°E. The total heat flux into the region is 3.62 TW, consisting of 0.87, 1.07, and 1.68 TW supplied by the mean, seasonal and eddy components of the circulation respectively (Table 1). While these values depend on where exactly we place the lateral boundaries for the integration, given that the ocean heat fluxes and air-sea fluxes balancing them vary along the shelf, how they change in response to seafloor roughness does not. In the SRTM15 simulation, the total heat flux into the shelf region drops to 3.45 TW with 1.01, 1.18, and 1.26 TW supplied by the mean, seasonal and eddy components, respectively. The response of the heat fluxes is consistent with the changes in the components of the circulation discussed above: the EKE is reduced along the shelf break, while the mean and seasonal circulation components of the ASC are increased in the SRTM15 simulation. Integrating the heat convergence for the ice cavity alone, defined as the region between the coastline and the ice shelf boundary we find 0.33 TW, consisting of 0.03, 0.14, and 0.16 TW supplied by the mean, seasonal and eddy components, respectively. In the SRTM15 simulation, the net heat convergence below the ice shelf reduces to 0.29 TW, consisting of 0.13 and 0.16 TW supplied by the seasonal and eddy circulation components and the mean circulation component making a negligible contribution.

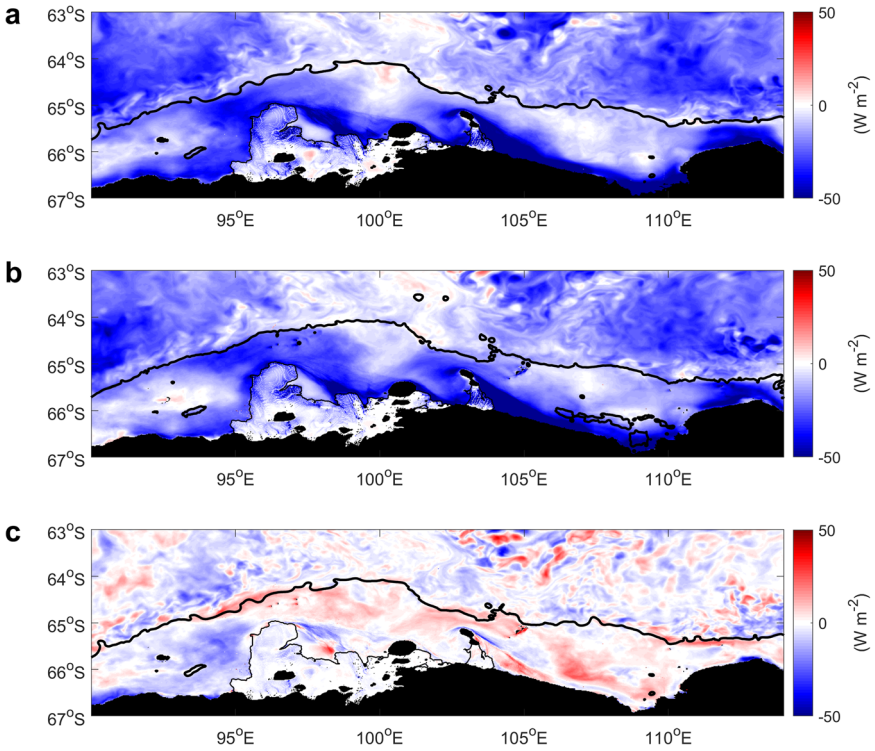

Fig. 5 | Ocean heat flux divergence. Divergence of time-averaged, vertically-integrated total ocean heat fluxes in (W m^{-2}) from (**a**) the BedMachine simulation and (**b**) the SRTM15 simulation. Negative divergence corresponds to convergence (source) of ocean heat fluxes. **c** Difference in magnitude of the energy convergence in (W m^{-2}) between the SRTM15 and BedMachine simulations. (thin black) Ice shelf boundary and (thick black) 1000 m isobath.

In summary, there is an overall convergence of the ocean heat fluxes over the continental shelf balanced by the local sinks of heat. Seafloor roughness makes an impact on the total heat transport across the shelf, reducing it by 0.17 TW, and affects the partitioning between the mean, seasonal, and eddy heat flux components. It also redistributes heat over the shelf: it results in a stronger heat flux convergence closer to the shelf break and upstream of the ice shelf and a weaker heat flux convergence near the coast and ice shelf front and to the west of the ice shelf. Within the cavity changes are more subtle. The total heat flux into the ice shelf cavities drops by 0.04 TW, or 12%, from 0.33 TW in the BedMachine simulation to 0.29 TW in the SRTM15 simulation.

Ice shelf melt rates

The decrease in the total ocean heat flux into the ice shelf cavities is balanced by a reduction in the heat consumption due to ice melting, and hence a reduction in melt rates. In the BedMachine simulation, melt rates (Fig. 6a) vary from 0 to 1 m yr^{-1} in the interior of the ice shelf to up to 4–5 m yr^{-1} at the edge. The Shackleton Ice Shelf and Denman Glacier are characterised by relatively high melt rates, whereas the Scott Glacier has low melt rates. These estimates are generally consistent with satellite estimates and previous modelling studies[12,18,72] (Supplementary Note 2). Integrated over the entire ice shelf, the BedMachine simulation melts 30 Gt yr^{-1}, which is somewhat lower but generally consistent with recent satellite-based estimate of 54.6 ± 7.2 Gt yr^{-1} for the Denman region[16]. The difference may be attributed to the uncertainty in the under-ice bathymetry[14] or discharge of subglacial melt water, a process not represented in the model[73,74]. In the SRTM15 simulation, melt rates reduce by up to 1 m yr^{-1} especially in the western part of the ice shelf around the Shackleton Ice Shelf (Fig. 6b, c), consistent with the reduction of the ocean heat flux convergence in that region. This reduction in melt rates amounts to a total meltwater discharge decrease of 4 Gt yr^{-1} in the SRTM15 simulation. An additional simulation with synthetic small-scale roughness over the shelf having the same spectral variance as in SRTM15 shows qualitatively similar changes in the local melt rates and a total meltwater discharge decrease of 2.5 Gt yr^{-1} (Supplementary Note 4). Increasing the variance of the synthetic roughness by a factor of two, as suggested by multi-beam soundings collected in the Vincennes Bay (Supplementary Note 1), leads to a stronger impact with a total meltwater discharge decrease of up to 8.3 Gt yr^{-1}.

Table 1 | Ocean heat fluxes

Region	Heat flux	BedMachine (TW)	SRTM15 (TW)	Difference (TW)/ percentage
Whole Shelf	THF	3.62	3.45	−0.17 (5%)
	MHF	0.87	1.01	0.14 (16%)
	SHF	1.07	1.18	0.11 (10%)
	EHF	1.68	1.26	−0.42 (25%)
Ice Shelf	THF	0.33	0.29	−0.04 (12%)
	MHF	0.03	0	−0.03 (100%)
	SHF	0.14	0.13	−0.01 (7%)
	EHF	0.16	0.16	0

Mean heat fluxes (MHF), seasonal heat fluxes (SHF), eddy heat fluxes (EHF) and total heat fluxes (THF) integrated for the whole shelf and the ice shelf boundaries in the BedMachine and SRTM15 simulations. Positive flux value corresponds to heat convergence in the region. Difference is computed as SRTM15 minus BedMachine; percentage is computed with respect to the reference (BedMachine) simulations.

Discussion

We explore the impact of seafloor roughness over the shelf on the ocean circulation, water mass properties, and glacial melt rates in the Denman region of Antarctica using a high-resolution regional model. Two simulations are carried out with two publicly available bathymetry products which differ primarily in their representation of small-scale bathymetry (seafloor roughness) in the region. Seafloor roughness is ubiquitous in the ocean and is dominated by O(10 km) scales[49]. While the impact of seafloor roughness can generally depend on the model resolution, we expect our results to hold qualitatively and quantitatively as long as these scales are resolved by the model.

We show that seafloor roughness makes an impact on the local ocean circulation, suppressing the mean AACC and eddies over the shelf and intensifying the ASC along the continental slope. As a result, the presence of

CDW over the shelf is reduced. Previous studies for the Southern Ocean show that it is the topographic form stress arising from seafloor roughness that impacts the large-scale motions such as currents and eddies[50,71]. Some of the topographic form stress is associated with the lee wave generation[75], while some can be associated with Rossby waves and other non-radiating motions generated by topographic features[76]. Internal tides have also been suggested to modulate lee waves and their impacts[77], in addition to driving tidal mixing in the interior[78]. With the resolution we use, 1.4 km in the horizontal and O(10 m) in the vertical, our model resolves the 10–100 km seafloor roughness scales well and thus is capable of resolving the dominant lee waves and internal tides generated by them. Hence, the model generally captures the dominant flow-topography interaction processes modifying the large-scale flows. Some of the processes, such as diapycnal mixing, may require additional parameterisations to relate the resolved velocity shears to turbulent mixing[79,80]. Disentangling the lee wave and internal tide effects over the continental shelf at the Antarctic margins is outside the scope of our study and will be addressed in future studies.

Our results suggest that unlike the ASC, the AACC does not act as a barrier, but instead facilitates heat transport. Changes in the properties and circulation over the continental shelf result in changes in heat transport towards the ice cavity. We find a stronger heat flux convergence (warming) at the outer part of the shelf and upstream of the ice shelf and weaker heat flux convergence (cooling) at the ice shelf front and west of the ice shelf. In turn, this leads to a reduction in ice shelf meltwater discharge of 4 Gt yr^{-1} in response to seafloor roughness. This meltwater reduction corresponds to a 14% change, and is comparable to the uncertainty in satellite-derived meltwater estimates for the Shackleton Ice Shelf/Denman Glacier system[16,18]. Available observations in Vincennes Bay suggest that SRTM15 underestimates the seafloor roughness over the shelf, implying that its impact on the circulation and ice shelf melting is also underestimated. Our additional simulation with synthetic roughness matching the observations shows up to 8.4 Gt yr^{-1}, or 28%, reduction in the total meltwater discharge (Supplementary Note 3 and 4).

Small-scale seafloor roughness that is absent in ocean and climate models can have a significant impact on the ocean circulation in the Antarctic margin, with effects on the heat transport towards ice shelf cavities, and ice sheet melting. Ocean thermal forcing is expected to increase under future climate[21]. Ice sheet melt rate parameterisations[81] and observations[82] suggest the melt rate response to temperature changes is non-linear, implying a strong sensitivity of basal melting to climate change in models[10]. Our study shows that seafloor roughness damps the ocean circulation over the continental shelf, reduces the CDW access to the ice shelf cavity, and suppresses melting. The suppressed melting, and hence meltwater production, further reduces the CDW access to the ice shelf cavity, suggesting that seafloor roughness can potentially reduce the model sensitivity to thermal forcing. Therefore, including the effect of seafloor roughness in climate models could potentially lead to a reduction in the spread of ice sheet melt rate estimates and sea level rise projections. In addition to potential improvements in coupled climate models, our results also have implications for high-resolution global and regional ocean models: resolved, or parameterised, small-scale seafloor roughness can improve the shelf circulation and water mass properties in those models. Finally, direct observations of the bathymetry around the Antarctic margins will be needed to account for seafloor roughness in high-resolution ocean models and guide the development of parameterisations for coupled climate models.

Methods

Regional model configuration

Our high-resolution regional model of the Shackleton Ice Shelf/Denman Glacier region is based on the Massachusetts Institute of Technology general circulation model (MITgcm)[83]. The model domain covers the region of 90–114°E and 60–67°S (Fig. 1). The model is configured with a 1/40° resolution in longitude and 1/80° resolution in latitude, corresponding to roughly 1.4 km. In the vertical, the model has 160 vertical levels ranging from 3 m vertical resolution at the surface to 100 m in the deep Southern Ocean; 100 vertical levels are used in the top 1 km to represent the continental shelf. The model has dynamic and thermodynamic sea ice components[84]. 4°-wide sponge layers are added at the eastern, western, and northern boundaries. Within the sponge layers the ocean and sea ice model fields are restored to monthly-mean fields from the 1990–91 repeat-year ACCESS-OM2-01 run[67]. The restoring time scale decreases from 3 months to 10 days within the sponge layers. The atmospheric forcing is derived from

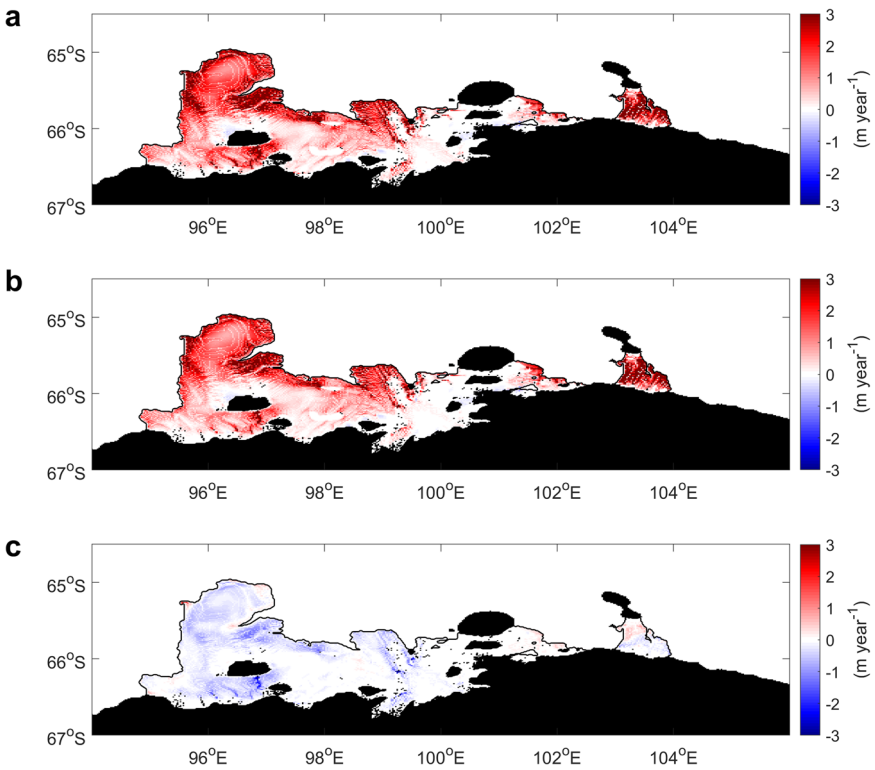

Fig. 6 | Ice shelf melt rate. Time-averaged ice shelf melt rate in (m yr^{-1}) from (**a**) the BedMachine simulation and (**b**) the SRTM15 simulation. **c** The difference of the ice shelf melt rate in (m yr^{-1}) between the SRTM15 and BedMachine simulations.

the Japanese 55-year atmospheric reanalysis (JRA55v1.3)[66] and applied 3-hourly. Tides are forced by applying TPXO9v4 barotropic tide velocities (https://www.tpxo.net/global/tpxo9-atlas) for 10 tidal constituents at the boundaries. The model has a thermodynamic ice shelf component[85]. Ice shelf freezing and melting is parameterised using the so-called three-equation ice shelf thermodynamics model[86,87]. The ice shelf geometry is generated using BedMachine Antarctica. The simulations are carried out with a quadratic bottom drag (2×10^{-3} drag coefficient) free-slip bottom boundary condition, a K-profile parameterisation, and Smagorinsky horizontal viscosity parameterisation for sub-grid scale processes.

We carry out and analyse two simulations configured using the seafloor bathymetry from BedMachine Antarctica and SRTM15. Bathymetry from BedMachine Antarctica is used in both simulations in a box region around the ice shelf (94.5-104°E, 64.8-67°S) to ensure that the geometry of the ice shelf cavities is identical in the two simulations. Our model only includes the Shackleton/Denman ice shelf and other cavities within the domain are not included. Both simulations are run for 10 years with the models reaching equilibrium after the first 5 years. The last 5 years of the model outputs are used for analysis. The regional model produces the large-scale ocean state consistent with its 'parent' model, ACCESS-OM2-01, which was previously validated in the Southern Ocean and for sea ice in Antarctica[67]. Shelf water properties also agree well with available float observations in the Denman region (Supplementary Note 2).

Decomposition of kinetic energy and heat fluxes

We decompose the total kinetic energy and heat fluxes into three components: mean, seasonal, and eddy components. The mean kinetic energy (MKE) is computed as

$$MKE = \frac{1}{2}\rho_0(u_m^2 + v_m^2), \quad (1)$$

where u_m and v_m are the time mean velocities computed as averages over the last 5 years of the simulation outputs, and ρ_0 is reference density of 1026 kg m^{-3}. The seasonal kinetic energy (SKE) is computed as

$$SKE = \frac{1}{2}\rho_0(u_s^2 + v_s^2), \quad (2)$$

where u_s and v_s are seasonal (monthly) velocity variability computed from monthly averaged velocities, $u_{monthly}$ and $v_{monthly}$, saved as model diagnostics

$$u_s = u_{monthly} - u_m, \quad \text{and} \quad v_s = v_{monthly} - v_m. \quad (3)$$

SKE is computed for each month and then averaged over the last 5 years of the simulations. Finally, the eddy kinetic energy (EKE) is computed by subtracting MKE and SKE from the total kinetic energy (KE) saved as a model diagnostic,

$$EKE = KE - MKE - SKE, \quad (4)$$

and also averaged over the last 5 years of the simulations. The heat flux components are computed in a similar way by using velocity and potential temperature model outputs.

Data availability

MITgcm model setup and data that support figures are available at https://doi.org/10.5281/zenodo.10819731. Full model outputs are available upon request to the corresponding author.

Code availability

MATLAB script that supports figures is available at https://doi.org/10.5281/zenodo.10819731.

Received: 8 October 2023; Accepted: 3 June 2024;
Published online: 13 June 2024

References

1. Intergovernmental Panel on Climate Change (IPCC). Climate Change 2021—The Physical Science Basis: Working Group I Contribution to the Sixth Assessment Report of the Intergovernmental Panel on Climate Change. https://doi.org/10.1017/9781009157896 (Cambridge University Press, 2023).
2. Jourdain, N. C. et al. A protocol for calculating basal melt rates in the ISMIP6 Antarctic ice sheet projections. *Cryosphere.* **14**, 3111–3134 (2020).
3. Lipscomb, W. H. et al. ISMIP6-based projections of ocean-forced Antarctic Ice Sheet evolution using the Community Ice Sheet Model. *Cryosphere.* **15**, 633–661 (2021).
4. Naughten, K. A. et al. Future projections of Antarctic ice shelf melting based on CMIP5 scenarios. *J. Clim.* **31**, 5243–5261 (2018).
5. Purich, A. & England, M. H. Historical and future projected warming of Antarctic Shelf Bottom Water in CMIP6 models. *Geophys. Res. Lett.* **48**, e2021GL092752 (2021).
6. Beadling, R. L. et al. Representation of Southern Ocean Properties Across Coupled Model Intercomparison Project Generations: CMIP3 to CMIP6. *J. Clim.* **33**, 6555–6581 (2020).
7. Wang, Z. & Meredith, M. P. Density-driven Southern Hemisphere subpolar gyres in coupled climate models. *Geophys. Res. Lett.* **35**, L14608 (2008).
8. Wang, Z. On the response of Southern Hemisphere subpolar gyres to climate change in coupled climate models. *J. Geophys. Res. Oceans.* **118**, 1070–1086 (2013).
9. Wang, Z. et al. On the multiscale oceanic heat transports toward the bases of the antarctic ice shelves. *Ocean-Land-Atmos Res.* **2**, 0010 (2023).
10. Li, D., DeConto, R. M. & Pollard, D. Climate model differences contribute deep uncertainty in future Antarctic ice loss. *Sci. Adv.* **9**, eadd7082 (2023).
11. Silvano, A., Rintoul, S. & Herraiz-Borreguero, L. Ocean-ice shelf interaction in East Antarctica. *Oceanogr.* **29**, 130–143 (2016).
12. Miles, B. W. J. et al. Recent acceleration of Denman Glacier (1972–2017), East Antarctica, driven by grounding line retreat and changes in ice tongue configuration. *Cryosphere.* **15**, 663–676 (2021).
13. Rignot, E. et al. Four decades of Antarctic Ice Sheet mass balance from 1979–2017. *PNAS* **116**, 1095–1103 (2019).
14. Brancato, V. et al. Grounding line retreat of Denman Glacier, East Antarctica, measured with COSMO-SkyMed radar interferometry data. *Geophys. Res. Lett.* **47**, e2019GL086291 (2020).
15. Flament, T. & Rémy, F. Dynamic thinning of Antarctic glaciers from along-track repeat radar altimetry. *J. Glaciol.* **58**, 830–840 (2012).
16. Liang, Q., Zhou, C. & Zheng, L. Mapping basal melt under the Shackleton ice shelf, East Antarctica, from CryoSat-2 radar altimetry. *IEEE J. Sel. Top. Appl. Earth Obs. Remote Sens.* **14**, 5091–5099 (2021).
17. Pritchard, H. et al. Antarctic ice-sheet loss driven by basal melting of ice shelves. *Nature* **484**, 502–505 (2012).
18. Rignot, E., Jacobs, S., Mouginot, J. & Scheuchl, B. Ice-shelf melting around Antarctica. *Science* **341**, 266–270 (2013).
19. Schmidtko, S., Heywood, K. J., Thompson, A. F. & Aoki, S. Multidecadal warming of Antarctic waters. *Science* **346**, 1227–1231 (2014).
20. Allen, S. E. & Durrieu de Madron, X. A review of the role of submarine canyons in deep-ocean exchange with the shelf. *Ocean Sci.* **5**, 607–620 (2009).
21. Jordan, J. R. et al. Increased warm water intrusions could cause mass loss in East Antarctica during the next 200 years. *Nat. Commun.* **14**, 1825 (2023).
22. Ribeiro, N. et al. Warm modified Circumpolar Deep Water intrusions drive ice shelf melt and inhibit Dense Shelf Water formation in

Vincennes Bay, East Antarctica. *J. Geophys. Res. Oceans* **126**, e2020JC016998 (2021).
23. Silvano, A. et al. Seasonality of warm water intrusions onto the continental shelf near the Totten Glacier. *J. Geophys. Res. Oceans* **124**, 4272–4289 (2019).
24. Bindoff, N., Rosenberg, M. & Warner, M. On the circulation and water masses over the Antarctic continental slope and rise between 80 and 150°E. *Deep-Sea Res. Pt. II* **47**, 2299–2326 (2000).
25. Herraiz-Borreguero, L. & Naveira Garabato, A. C. Poleward shift of Circumpolar Deep Water threatens the East Antarctic Ice Sheet. *Nat. Clim. Change* **12**, 728–734 (2022).
26. Thompson, A. F., Stewart, A. L., Spence, P. & Heywood, K. J. The Antarctic Slope Current in a changing climate. *Rev. Geophys.* **56**, 741–770 (2018).
27. Nakayama, Y. et al. Antarctic slope current modulates ocean heat intrusions towards Totten Glacier. *Geophys. Res. Lett.* **48**, e2021GL094149 (2021).
28. Nøst, O. A. et al. Eddy overturning of the Antarctic Slope Front controls glacial melting in the Eastern Weddell Sea. *J. Geophys. Res. Oceans* **116**, C11014 (2011).
29. Stewart, A. L. & Thompson, A. F. Eddy-mediated transport of warm Circumpolar Deep Water across the Antarctic shelf break. *Geophys. Res. Lett.* **42**, 432–440 (2015).
30. Flexas, M. M., Schodlok, M. P., Padman, L., Menemenlis, D. & Orsi, A. H. Role of tides on the formation of the Antarctic Slope Front at the Weddell-Scotia Confluence. *J. Geophys. Res. Oceans* **120**, 3658–3680 (2015).
31. Stewart, A. L., Klocker, A. & Menemenlis, D. Circum-Antarctic shoreward heat transport derived from an eddy-and tide-resolving simulation. *Geophys. Res. Lett.* **45**, 834–845 (2018).
32. Jacobs, S. S. On the nature and significance of the Antarctic Slope Front. *Mar. Chem.* **35**, 9–24 (1991).
33. Schubert, R., Thompson, A. F., Speer, K., Schulze Chretien, L. & Bebieva, Y. The Antarctic coastal current in the Bellingshausen Sea. *Cryosphere* **15**, 4179–4199 (2021).
34. Friedrichs, D. M. et al. Observations of submesoscale eddy-driven heat transport at an ice shelf calving front. *Commun. Earth Environ.* **3**, 140 (2022).
35. Makinson, K. Modeling tidal current profiles and vertical mixing beneath Filchner-Ronne Ice Shelf, Antarctica. *J. Phys. Oceanogr.* **32**, 202–215 (2002).
36. Hellmer, H. H., Kauker, F., Timmermann, R., Determann, J. & Rae, J. Twenty-first-century warming of a large Antarctic ice-shelf cavity by a redirected coastal current. *Nature* **485**, 225–228 (2012).
37. Sun, C. et al. On the influences of the continental shelf bathymetry correction in Prydz Bay, East Antarctica. *Front. Mar. Sci.* **9**, 957414 (2022).
38. Holland, P. R., Jenkins, A. & Holland, D. M. Ice and ocean processes in the Bellingshausen Sea, Antarctica. *J. Geophys. Res.* **115**, C05020 (2010).
39. Moffat, C., Beardsley, R. C., Owens, B. & van Lipzig, N. A first description of the Antarctic Peninsula Coastal Current. *Deep Sea Res. Part II* **55**, 277–293 (2008).
40. Nakayama, Y. et al. Pathways of ocean heat towards Pine Island and Thwaites grounding lines. *Sci. Rep.* **9**, 16649 (2019).
41. Jacobs, S. et al. The Amundsen Sea and the Antarctic ice sheet. *Oceanography* **25**, 154–163 (2012).
42. Walker, D. P. et al. Oceanic heat transport onto the Amundsen Sea shelf through a submarine glacial trough. *Geophys. Res. Lett.* **34**, L02602 (2007).
43. Liu, C. et al. On the modified Circumpolar Deep Water upwelling over the Four Ladies Bank in Prydz Bay, East Antarctica. *J. Geophys. Res. Oceans* **123**, 7819–7838 (2018).
44. van Wijk, E. M., Rintoul, S. R., Wallace, L. O., Ribeiro, N. & Herraiz-Borreguero, L. Vulnerability of Denman Glacier to ocean heat flux revealed by profiling float observations. *Geophys. Res. Lett.* **49**, e2022GL100460 (2022).
45. Liu, C. et al. Topography-mediated transport of warm deep water across the Continental Shelf Slope, East Antarctica. *J. Phys. Oceanogr.* **52**, 1295–1314 (2022).
46. Haigh, M., Holland, P. R. & Jenkins, A. The influence of bathymetry over heat transport onto the Amundsen Sea continental shelf. *J. Geophys. Res. Oceans* **128**, e2022JC019460 (2023).
47. Rintoul, S. R. et al. Ocean heat drives rapid basal melt of the Totten Ice Shelf. *Sci. Adv.* **2**, e1601610 (2016).
48. Hogan, K. A. et al. Revealing the former bed of Thwaites Glacier using sea-floor bathymetry: implications for warm-water routing and bed controls on ice flow and buttressing. *Cryosphere* **14**, 2883–2908 (2020).
49. Goff, J. A., Smith, W. H. & Marks, K. M. The contributions of abyssal hill morphology and noise to altimetric gravity fabric. *Oceanography* **17**, 24–37 (2004).
50. Zhang, X. & Nikurashin, M. Small-scale topographic form stress and local dynamics of the Southern Ocean. *J. Geophys. Res. Oceans* **125**, e2019JC015420 (2020).
51. Trossman, D. S. et al. Impact of parameterized lee wave drag on the energy budget of an eddying global ocean model. *Ocean Model.* **72**, 119–142 (2013).
52. Trossman, D. S. et al. Impact of topographic internal lee wave drag on an eddying global ocean model. *Ocean Model.* **97**, 109–128 (2016).
53. Yang, L., Nikurashin, M., Hogg, A. M. & Sloyan, B. M. The impact of lee waves on the Southern Ocean circulation. *J. Phys. Oceanogr.* **51**, 2933–2950 (2021).
54. Marshall, D. P., Ambaum, M. H. P., Maddison, J. R., Munday, D. R. & Novak, L. Eddy saturation and frictional control of the Antarctic Circumpolar Current. *Geophys. Res. Lett.* **44**, 286–292 (2017).
55. Yang, L., Nikurashin, M., Hogg, A. M. & Sloyan, B. M. Lee waves break eddy saturation of the Antarctic Circumpolar Current. *Geophys. Res. Lett.* **50**, e2023GL103866 (2023).
56. Melet, A., Hallberg, R., Legg, S. & Nikurashin, M. Sensitivity of the ocean state to Lee wave-driven mixing. *J. Phys. Oceanogr.* **44**, 900–921 (2014).
57. Nikurashin, M. & Ferrari, R. Radiation and dissipation of internal waves generated by geostrophic motions impinging on small-scale topography: application to the Southern Ocean. *J. Phys. Oceanogr.* **40**, 2025–2042 (2010).
58. Nikurashin, M. & Ferrari, R. Overturning circulation driven by breaking internal waves in the deep ocean. *Geophys. Res. Lett.* **40**, 3133–3137 (2013).
59. Howat, I. M., Porter, C., Smith, B. E., Noh, M.-J. & Morin, P. The reference elevation model of Antarctica. *Cryosphere* **13**, 665–674 (2019).
60. Morlighem, M. et al. Deep glacial troughs and stabilizing ridges unveiled beneath the margins of the Antarctic ice sheet. *Nat. Geosci.* **13**, 132–137 (2020).
61. Sandwell, D. T. et al. Improved bathymetric prediction using geological information: SYNBATH. *Earth Space Sci.* **9**, e2021EA002069 (2022).
62. Morlighem, M. MEaSUREs BedMachine Antarctica, Version 2. *NASA National Snow and Ice Data Center Distributed Active Archive Center* https://doi.org/10.5067/E1QL9HFQ7A8M (2020).
63. Arndt, J. E. et al. The International Bathymetric Chart of the Southern Ocean (IBCSO) Version 1.0-A new bathymetric compilation covering circum-Antarctic waters. *Geophys. Res. Lett.* **40**, 3111–3117 (2013).
64. Tozer, B. et al. Global bathymetry and topography at 15 arc sec: SRTM15+. *Earth Space Sci.* **6**, 1847–1864 (2019).
65. Dorschel, B. et al. The International Bathymetric Chart of the Southern Ocean Version 2. *Sci. Data* **9**, 275 (2022).
66. Tsujino, H. et al. JRA-55-based surface dataset for driving ocean-sea-ice models (JRA55-do). *Ocean Model.* **130**, 79–139 (2018).
67. Kiss, A. E. et al. ACCESS-OM2 v1. 0: a global ocean-sea ice model at three resolutions. *Geosci. Model Dev.* **13**, 401–442 (2020).

68. Nitsche, F. O. et al. Bathymetric control of warm ocean water access along the East Antarctic Margin. *Geophys. Res. Lett.* **44**, 8936–8944 (2017).
69. Walker, A. & Pedlosky, J. Instability of meridional baroclinic currents. *J. Phys. Oceanogr.* **32**, 1075–1093 (2002).
70. Mack, S. L., Dinniman, M. S., Klinck, J. M., McGillicuddy, D. J. & Padman, L. Modeling ocean eddies on Antarctica's cold water continental shelves and their effects on ice shelf basal melting. *J. Geophys. Res. Oceans* **124**, 5067–5084 (2019).
71. Nikurashin, M., Vallis, G. K. & Adcroft, A. Routes to energy dissipation for geostrophic flows in the Southern Ocean. *Nat. Geosci.* **6**, 48–51 (2013).
72. Depoorter, M. A. et al. Calving fluxes and basal melt rates of Antarctic ice shelves. *Nature* **502**, 89–92 (2013).
73. Gwyther, D. E., Dow, C. F., Jendersie, S., Gourmelen, N. & Galton-Fenzi, B. K. Subglacial freshwater drainage increases simulated basal melt of the Totten Ice Shelf. *Geophys. Res. Lett.* **50**, e2023GL103765 (2023).
74. Nakayama, Y., Cai, C. & Seroussi, H. Impact of subglacial freshwater discharge on Pine Island Ice Shelf. *Geophys. Res. Lett.* **48**, e2021GL093923 (2021).
75. Naveira Garabato, A. C., Nurser, A. J., Scott, R. B. & Goff, J. A. The impact of small-scale topography on the dynamical balance of the ocean. *J. Phys. Oceanogr.* **43**, 647–668 (2013).
76. Klymak, J. M. et al. Nonpropagating form drag and turbulence due to stratified flow over large-scale abyssal hill topography. *J. Phys. Oceanogr.* **48**, 2383–2395 (2018).
77. Shakespeare, C. J. et al. Interdependence of internal tide and Lee wave generation at abyssal hills: global calculations. *J. Phys. Oceanogr.* **50**, 655–677 (2020).
78. Polzin, K. L., Toole, J. M., Ledwell, J. R. & Schmitt, R. W. Spatial variability of turbulent mixing in the abyssal ocean. *Science* **276**, 93–96 (1997).
79. Jackson, L., Hallberg, R. & Legg, S. A parameterization of shear-driven turbulence for ocean climate models. *J. Phys. Oceanogr.* **38**, 1033–1053 (2008).
80. St. Laurent, L. & Garrett, C. The role of internal tides in mixing the deep ocean. *J. Phys. Oceanogr.* **32**, 2882–2899 (2002).
81. Holland, P. R., Jenkins, A. & Holland, D. M. The response of ice shelf basal melting to variations in ocean temperature. *J. Clim.* **21**, 2558–2572 (2008).
82. Jenkins, A. et al. West Antarctic Ice Sheet retreat in the Amundsen Sea driven by decadal oceanic variability. *Nat. Geosci.* **11**, 733–738 (2018).
83. Marshall, J., Adcroft, A., Hill, C., Perelman, L. & Heisey, C. A finite-volume, incompressible Navier Stokes model for studies of the ocean on parallel computers. *J. Geophys. Res. Oceans* **102**, 5753–5766 (1997).
84. Losch, M., Menemenlis, D., Campin, J.-M., Heimbach, P. & Hill, C. On the formulation of sea-ice models. Part 1: Effects of different solver implementations and parameterizations. *Ocean Model.* **33**, 129–144 (2010).
85. Losch, M. Modeling ice shelf cavities in a z coordinate ocean general circulation model. *J. Geophys. Res.* **113**, C08043 (2008).
86. Hellmer, H. H. & Olbers, D. J. A two-dimensional model for the thermohaline circulation under an ice shelf. *Antarct. Sci.* **1**, 325–336 (1989).
87. Holland, D. M. & Jenkins, A. Modeling thermodynamic ice-ocean interactions at the base of an ice shelf. *J. Phys. Oceanogr.* **29**, 1787–1800 (1999).

Acknowledgements

This work was supported in part by funding from the Australian Government as part of the Antarctic Science Collaboration Initiative programme, through the Australian Antarctic Program Partnership. This research was also supported by the Australian Research Council Special Research Initiative, Australian Centre for Excellence in Antarctic Science (Project Number SR200100008). This research was undertaken on the NCI National Facility in Canberra, Australia.

Author contributions

Y.L. led the analysis of the results and writing of the paper. M.N. performed the simulations, contributed to the interpretation of the results, and was responsible for the design of the study. B.P.M. contributed to the design of the study and interpretation of the results. Y.L., M.N., and B.P.M. contributed to the discussion of the results and writing of the paper.

Competing interests

The authors declare no competing interests.

Additional information

Supplementary information The online version contains supplementary material available at https://doi.org/10.1038/s43247-024-01480-x.

Correspondence and requests for materials should be addressed to Beatriz Peña-Molino.

Peer review information *Communications Earth & Environment* thanks Lois Baker, Zhaomin Wang and the other, anonymous, reviewer(s) for their contribution to the peer review of this work. Primary Handling Editors: Viviane Menezes, Joe Aslin and Aliénor Lavergne. A peer review file is available.